Journal of Alloys and Compounds 813 (2020) 152245

Contents lists available at ScienceDirect

Journal of Alloys and Compounds

journal homepage: http://www.elsevier.com/locate/jalcom

Structural transition, electrical and magnetic properties of Cr doped $Bi_{0.9}Sm_{0.1}FeO_3$ multiferroics

P.T. Phong [a, b], N.H. Thoan [c], N.T.M. Hong [d], N.V. Hao [e], L.T. Ha [f], T.N. Bach [g], T.D. Thanh [g], C.T.A. Xuan [e], N.V. Quang [h], N.V. Dang [e], T.A. Ho [d], P.T. Tho [e, *]

[a] Laboratory of Magnetism and Magnetic Materials, Advanced Institute of Materials Science, Ton Duc Thang University, Ho Chi Minh City, Viet Nam
[b] Faculty of Applied Sciences, Ton Duc Thang University, Ho Chi Minh City, Viet Nam
[c] School of Engineering Physics, Ha Noi University of Science and Technology, Ha Noi, Viet Nam
[d] Faculty of Engineering Physics and Nanotechnology, VNU University of Engineering and Technology, Ha Noi, Viet Nam
[e] Department of Physics and Technology, Thai Nguyen University of Sciences, Thai Nguyen, Viet Nam
[f] Institute of Research and Development, Duy Tan University, Da Nang, 550000, Viet Nam
[g] Institute of Materials Science, VAST, 18-Hoang Quoc Viet, Ha Noi, Viet Nam
[h] Faculty of Chemistry, Ha Noi Pedagogical University 2, Vinh Phuc, Viet Nam

ARTICLE INFO

Article history:
Received 14 June 2019
Received in revised form
9 September 2019
Accepted 10 September 2019
Available online 11 September 2019

Keywords:
$BiFeO_3$
Crystal structure
Magnetic properties

ABSTRACT

The structural, vibrational, electrical and magnetic properties of $Bi_{0.9}Sm_{0.1}Fe_{1-x}Cr_xO_3$ ($0.02 \leq x \leq 0.1$) ceramics have been investigated in the vicinity of the morphotropic phase boundary (MPB) between the rhombohedral and orthorhombic structures. X-ray diffraction (XRD) patterns reveal a gradual formation of the orthorhombic phase and $Bi_{14}CrO_{24}$ impurity with increasing chromium concentration. The Rietveld refinement and Raman scattering analysis confirm the structural transformation from the polar *R3c* to the anti-polar *Pnam* phases. The Cole-Cole plots show two relaxation regimes which are attributed to gain and grain boundary responses above room temperature. The slim magnetic hysteresis loops are observed in samples with $x = 0.02-0.08$, while a robust loop with the coercivity field of $H_c \approx 1200$ Oe is observed for $x = 0.1$ sample where the canted antiferromagnetic phase is significantly contributed to the total magnetization. This result approves that the cycloidal spin structure cannot be suppressed by Cr doping.

1. Introduction

Multiferroic materials exhibiting morphotropic phase boundary (MPB) have attracted extensive attention due to their fascinating fundamental physics as well as their potentials candidate for device applications [1–5]. In general, an MPB is characterized by the coexistence of two different structural phases with a flattening of Gibbs free energy profile near the phase boundary [6,7]. The phase coexistence with the difference in lattice strain and anti/ferroelectric orderings often displays superior piezoelectric response and enhanced ferroelectric properties [5,8–10]. It is well-known that the anomalous enhancement of the piezoelectric response in the MPB systems stems from the intrinsic lattice strain of the bridging phase or electric-field-driven reversible antipolar to polar phase transformation [1,4,5,10,11]. Even though MPB multiferroic systems are very interesting from a piezoelectric application point of view, their magnetic properties have yet achieved any prominent results. The magnetic properties of $BiFeO_3$-based ceramic compounds only show a weak ferromagnetic behavior which has maximum saturation magnetization (M_s) of 0.5 emu/g for bulk ceramics [12]. At the MPB, the coexistence of the canted antiferromagnetic phase and the cycloidal spin structure of the *R3c* phase is contributed to the weak ferromagnetism of $BiFeO_3$ (BFO) systems [13]. More recently, we have experimentally observed a variation in magnetization of (La,Ti) codoped BFO ceramics for which the magnetization measured after few months has increased four times larger than that for as-prepared sample [14]. We have proposed that the phase boundary ferromagnetism induced by spin frustration at the phase boundary has been responsible for the variation happened in magnetization of BFO-based compounds [15,16]. The spin frustration may concern to the reconstruction of spin structure

* Corresponding author. Department of Physics and Technology, Thai Nguyen University of Sciences, Thai Nguyen, Viet Nam.
E-mail addresses: phamthanhphong@tdtu.edu.vn (P.T. Phong), thopt@tnus.edu.vn (P.T. Tho).

https://doi.org/10.1016/j.jallcom.2019.152245
0925-8388/

because of the structural instability at the MPB [8,17–19]. The phase boundary ferromagnetism can explain not only the abnormal magnetic properties but also the exchange bias effect and the vertical hysteresis shift observed at the MPB of BFO-based ceramic compounds [15,16,20–22]. Indeed, the phase boundary has a smooth interface, which can be a good support for the magnetic coupling of two structures with the distinct magnetic anisotropies [4,23,24]. Therefore, controlling the phase boundary ferromagnetism could be the key to overcome the final drawback, which is the weak ferromagnetism, of BFO. To date, a lot of effort has been dedicated to reveal a correlation between the crystal structure and the ferroelectric/ferromagnetic properties of Sm doped BFO, especially at the MPB [2,4,10,23–25]. At room temperature $Bi_{1-y}Sm_yFeO_3$ compounds retain a single polar *R3c* structure for samarium concentration of $y \leq 0.1$. The system then shows the polymorphs of the polar *R3c* and antipolar $PbZrO_3$-type orthorhombic structures for composition in the range of $0.1 < y < 0.18$. At the critical composition of y ~0.18, the system finally transforms into the nonpolar *Pbnm* structure (isostructural with $SmFeO_3$) [10,17,26]. The $Bi_{1-y}Sm_yFeO_3$ system at the polar rhombohedral and antipolar orthorhombic phase boundary is of particular interest since the phase coexistence can enhance the piezoelectric, ferroelectric and magnetic properties [2,13,25,27]. On the other hand, various reports on Sm and transition metal codoped BFO are also available in other related references [25,28–30]. We believe that, to this day, there are however no reports on (Sm,Cr) codoped BFO. This motivated us to study the structural transition and magnetic properties of Cr doped $Bi_{0.9}Sm_{0.1}FeO_3$ at the phase boundary of the rhombohedral and orthorhombic structures.

2. Experimental details

Polycrystalline compounds of the form $Bi_{0.9}Sm_{0.1}Fe_{1-x}Cr_xO_3$ (BSFCO) with $x = 0.02–0.1$ were prepared by a conventional solid-state reaction. High-purity (99.9%) Bi_2O_3, Sm_2O_3, Fe_2O_3, and Cr_2O_3 powders were used as precursors. These powders, which have specific composition, were mixed, carefully ground, and then pre-annealed at 850 °C in air for 24 h. The pre-annealed samples were re-ground, pressed into pellets, and finally sintered in air at 930 °C for 12 h. The crystalline structure and phonon characteristics of the fabricated samples were studied by using an X-ray diffractometer (Miniflex Rigaku) equipped with a Cu-Kα radiation source ($\lambda = 1.5405$ Å), and Raman scattering spectroscopy (LabRAM HR Evolution, Horiba) with excitation wavelength of $\lambda = 532$ nm. The morphology and composition of the samples were examined by scanning electron microscope (Hitachi S − 4800). Temperature dependent impedance spectroscopy was done from room temperature to 260 °C, in air, using a HP 4192A LF impedance analyzer. The XRD data were analyzed by the Rietveld method using the GSAS-2 program. Magnetization measurements were performed on a VSM LakeShore 7400. All investigations were carried out at room temperature.

3. Results and discussion

Fig. 1 shows the XRD patterns at room temperature of the BSFCO samples. The diffraction patterns of $x = 0.02$, and 0.04 samples are well identified according to the *R3c* rhombohedral structure of BFO. These other samples show a phase coexistence of two perovskite structures, which are concerned with the structural transition from the *R3c* rhombohedral to $PbZrO_3$-type orthorhombic structures. The appearance of the orthorhombic phase can be clearly seen in the diffraction pattern of $x = 0.1$ sample for which the Miller indices of the *R3c* phase and diffraction peaks of the $PbZrO_3$-like phase have been denoted in Fig. 1. Besides two structural phases, we

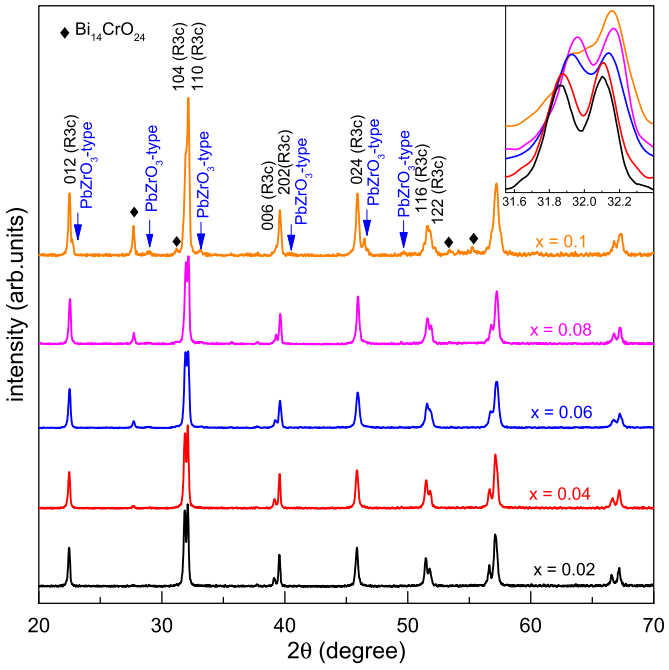

Fig. 1. XRD patterns of BSFCO samples. The inset shows the diffraction peaks at around 32^0.

observe an increase in intensity of the diffraction peaks of $Bi_{14}CrO_{24}$ impurity with increasing Cr concentration. The crystal structure of $Bi_{14}CrO_{24}$ phase belongs to the body centered tetragonal (*I4/m*) structure with unit cell parameters a ~8.7 Å and c ~ 17.3 Å [31]. The formation of $Bi_{14}CrO_{24}$ impurity in Cr doped BFO-based compounds is very difficult to avoid during high temperature sintering at ambient pressure [32,33]. In addition, the inset of Fig. 1 also reveals that the diffraction patterns have an obvious shift toward a high angle, meaning that the incorporation of Cr^{3+} (0.615 Å) ions at Fe^{3+} (0.645 Å) site of BSFCO compounds causes a slight volume shrinkage of the *R3c* rhombohedral unit cell. As mentioned above, the $Bi_{1-y}Sm_yFeO_3$ compounds show a phase separation between the *R3c* rhombohedral and the *Pbam* (or *Pnam*) orthorhombic structures at the critical composition of y ~ 0.1 [2,24,34]. Both the *Pbam* and *Pnam* space groups are used to assign the crystal symmetry of the $PbZrO_3$-type structure of $Bi_{1-y}Sm_yFeO_3$ compounds because of their very similar appearance in x-ray and neutron diffraction. In fact, the different in two space groups can be exposed by spatially local electron diffraction measurements [35]; however, the symmetry assignment of the $PbZrO_3$-type orthorhombic structure of Sm doping still remains controversial [2,4,23,34,36]. For this reason, $PbZrO_3$-type was used to denote either the *Pbam* or *Pnam* orthorhombic structures for our samples. To further clarify the structural transformation, we did a simulation on the crystal structure of BSFCO samples by using the Rietveld refinement method. The refinement was performed adopting the *R3c* + *Pnam* (or *Pbam*) models for $x = 0.02$ and *R3c* + *Pnam* (or *Pbam*) + *I4/m* models for $x = 0.04–0.1$. It is worth noting that the *Pnam* and *Pbam* has respectively lattice parameters $\sqrt{2}a_c \times 2\sqrt{2}a_c \times 4a_c$ and $\sqrt{2}a_c \times 2\sqrt{2}a_c \times 2a_c$, where $a_c \approx 4$ Å is the pseudocubic lattice parameter. As seen in Fig. 2, the Rietveld refinement using either the *R3c* + *Pnam* + *I4/m* or *R3c* + *Pbam* + *I4/m* models produces comparable fitting quality, confirming that it is not possible to distinguish the two orthorhombic symmetry through Rietveld refinement. Therefore, in this report, we only show the structural parameter and weight fraction of the refinement employing the

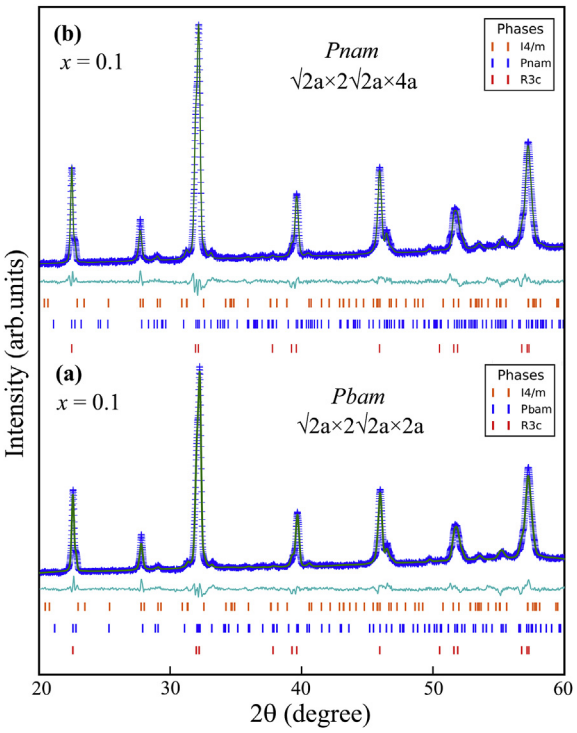

Fig. 2. Rietveld refined XRD patterns of sample $x = 0.1$ using (a) *Pbam* model ($\sqrt{2}a \times 2\sqrt{2}a \times 2a$) and (b) *Pnam* model (a $\sqrt{2}a \times 2\sqrt{2}a \times 4a$).

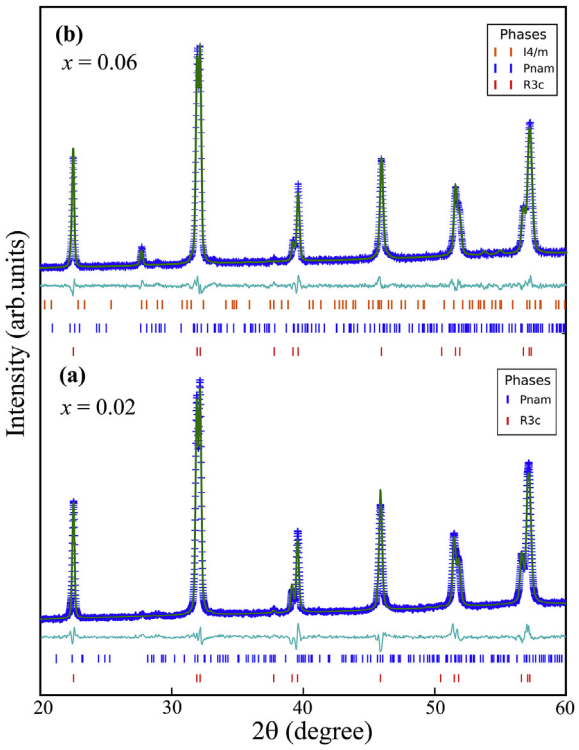

Fig. 3. Rietveld refined XRD patterns of samples (a) $x = 0.02$ and (b) $x = 0.06$.

R3c + *Pnam* + *I4/m* model (Table 1). The Rietveld refined XRD patterns of samples $x = 0.02$ and 0.06 are shown in Fig. 3. It is clear that all the diffraction peaks are well fitted to the suggested phase models.

Fig. 4 shows the room temperature Raman spectra of BSFCO compounds excited by a 532 nm wavelength. At low doping concentration, vibrational modes are well consistent with the Raman active modes of the *R3c* rhombohedral of BFO [37,38]. For instance, for $x = 0.02$, there are clearly nine Raman modes observed at 142, 173, 233, 242, 262, 278, 480, 530, and 630 cm^{-1} corresponding to A_1-(TO), E_2-(LO), A_1-2 (TO), E−3 (LO), E−4 (TO), E−5 (TO), E−8 (LO), E−9 (TO), and E−9 (LO) [37]. Furthermore, there are three phonon modes located over 900 cm^{-1}, among which two modes at 1106 and 1267 cm^{-1} are related to the second-order scattering of the *R3c* phase in BSFCO compounds [38]; while the peak at 828 cm^{-1} is a phonon vibration of the *I4/m* symmetry of $Bi_{14}CrO_{24}$ impurity.

Table 1
The crystal symmetry and lattice parameters of $^{Bi0.9Sm0.1Fe1-xCrxO3}$ compounds. The *I4/m* space group correspond to $Bi_{14}CrO_{24}$ impurity.

Composition	Space group	*a* (Å)	*b* (Å)	*c* (Å)	*V* (Å)^3
$x = 0.02$	*R3c* (98%)	5.5656	5.5656	13.7916	369.97
	Pnam (2%)	5.5962	11.2661	15.6304	985.45
$x = 0.04$	*R3c* (94%)	5.5633	5.5633	13.7827	369.43
	Pnam (4%)	5.5863	11.2281	15.6296	980.35
	I4/m (2%)	8.6912	8.6912	17.2076	1299.83
$x = 0.06$	*R3c* (90%)	5.5642	5.5642	13.7767	369.38
	Pnam (6%)	5.5750	11.1935	15.6266	975.15
	I4/m (4%)	8.7158	8.7158	17.1342	1301.60
$x = 0.08$	*R3c* (83%)	5.5637	5.5637	13.7758	369.29
	Pnam (9%)	5.5739	11.1901	15.6255	974.60
	I4/m (8%)	8.7036	8.7036	17.1441	1298.71
$x = 0.1$	*R3c* (63%)	5.5646	5.5646	13.7657	369.15
	Pnam (27%)	5.5726	11.1899	15.6253	974.36
	I4/m (10%)	8.6935	8.6935	17.1577	1296.72

Generally, the vibration of Bi−O covalent bonds contributes to the phonon frequency below 200 cm^{-1}, and thus the redshift of the A_1-(TO) mode and blueshift of the E_2-(LO) mode indicate that the substitution of Cr ions for Fe can cause a distortion of the *R3c* phase. In addition, the A_1-(TO) and E_2-(LO) Raman modes show sharp peaks with high intensity in all samples approve a conservation of the ferroelectric long-range ordering in BSFCO samples [39]. A further increase in Cr concentration may suppress the ferroelectric properties of compounds because both the A_1-(TO) and E_2-(LO) peaks are broadened and their intensities get weaker at the MPB of rhombohedral and orthorhombic structures [38,40,41], as observed in sample $x = 0.1$. Therefore, the phase transition from the polar *R3c* to the antipolar orthorhombic structures should be presented in our samples. Besides, the presence of the orthorhombic phase in BSFCO samples can also be confirmed by the emergence of a new peak at around 107 cm^{-1} in the sample $x = 0.1$, as seen in the inset of Fig. 4(b). Our observation is very well consistent with previous reports on Sm doped BFO [42,43]. Though the Raman scattering spectra is very sensitive to the structural transition, however, the lattice vibrations of two distinct symmetry at the MPB generally shows overlapping peaks in the Raman spectra, preventing phonon assignment for individual symmetry. Therefore, except for the mode located at 107 and 252 cm^{-1}, we did not observe other modes belonging to the orthorhombic structure in Fig. 4. It is clear that all the modes are well conserved in the Raman spectra of BSFCO compounds, proving the existence of *R3c* symmetry throughout the composition range $0.02 \leq x \leq 0.1$. A broad band (200−300 cm^{-1}) observed in Fig. 4(a) can be deconvoluted into five individual Lorentzian components, as clearly seen in the inset of Fig. 4(a) for $x = 0.02$ and the inset of Fig. 4(b) for $x = 0.1$. The A_1-2 (TO) mode is a vibrational characteristic of FeO_6 octahedral, and its frequency is strongly dependent on the octahedral tilt angle along [111] direction of *R3c* symmetry [38]. The tilt mode frequency of $Bi_{0.9}Sm_{0.1}Fe_{0.98}Cr_{0.02}O_3$ ($x = 0.02$) sample is about 233 cm^{-1}, which

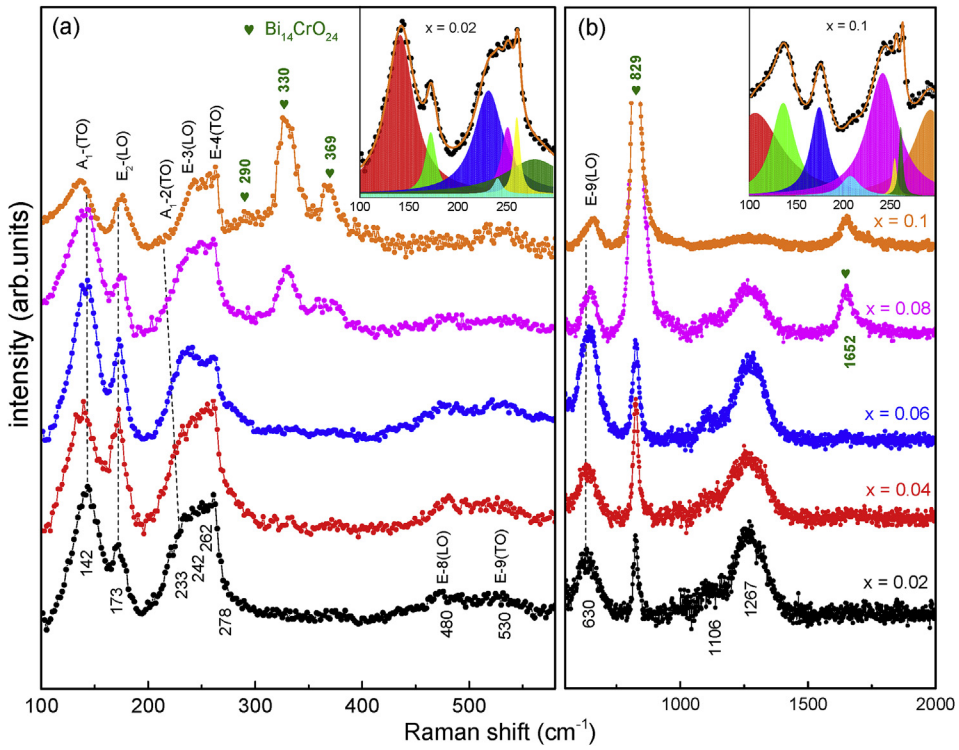

Fig. 4. RS spectra of BSFCO samples in the spectral range (a) 100–580 cm^{-1} and (b) 550–2000 cm^{-1}. The inset of Fig. 4(a) and (b) show respectively deconvoluted Raman spectra for $x = 0.02$ and 0.1 in the region of 100–300 cm^{-1}.

is good in agreement with that of 234 cm^{-1} for $Bi_{0.9}Sm_{0.1}FeO_3$ [38] and 236 cm^{-1} for $Bi_{0.825}Sm_{0.175}FeO_3$ [42]. Upon increasing the amount of Cr, the tilt mode shifts obviously toward lower frequency. The tilt mode frequency dependence of Cr concentration is plotted in Fig. 5. It was found that the decrease of [111] tilt angle is proportional to the redshift of the tilt mode with a slope of 18 cm^{-1}/tilt deg [38]. Here, the tilt mode frequency changed from 233 cm^{-1} in sample $x = 0.02$ to 209 cm^{-1} in sample $x = 0.1$, corresponding 24 cm^{-1} shifted-frequency of the tilt mode. Thus, the tilt angle is expected to decrease by ~1.3°. Due to the dependence of Dzyaloshinskii–Moriya interactions on the tilt angle and the deviation of $Fe^{3+} - O - Fe^{3+}$ bond angle from 180°, the change in tilt angle will strongly affect the magnetic properties of BSFCO samples [44,45]. It is worth noting that the Raman vibrations of $Bi_{14}CrO_{24}$ impurity have never been reported. However, there is no doubt to assign the Raman modes at 290, 330, 369, 829, and 1652 cm^{-1}, which is marked by heart symbol in Fig. 4, to the phonon vibrations of $Bi_{14}CrO_{24}$.

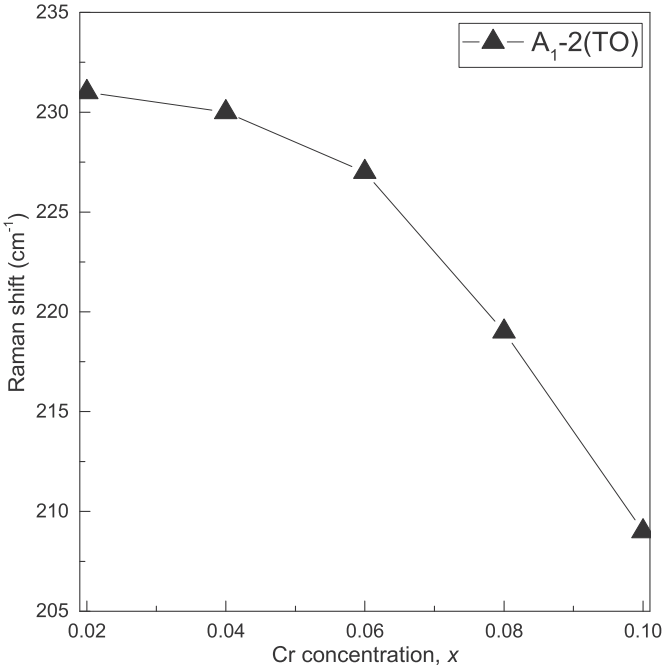

Fig. 5. Position of the A_1-2 (TO) tilt mode as a function of Cr concentration.

Fig. 6 shows the typical SEM micrographs of BSFCO samples. The micrographs clearly exhibit the polycrystalline nature of ceramic samples with non-uniform in gain sizes and shapes. At low doping concentration, the micrographs of samples $x = 0.02$ and 0.04 show typical polygonal shape with a grain size varying from 40 to 80 μm for $x = 0.02$ and 30–40 μm for $x = 0.04$. With Cr addition, polygonal grain shapes are transformed into cubic grains with a remarkably reduced grain size from 30 to 45 μm for $x = 0.06$ and 15–20 μm for $x = 0.1$. It can be inferred that Cr doping inhibits grain growth and leads to a transformation of grain shape. The reduction of grain size may originate from the suppression of oxygen vacancies or the phase coexistence in BSFCO compounds. The fine grains observed in Fig. 6(c) can be referred to the morphology of $Bi_{14}CrO_{24}$ impurity. The change of morphology may greatly impact on the electrical and ferroelectric properties of our samples.

Fig. 7 shows the complex impedance plots (Cole-Cole) for BSFCO samples in the temperature range of 30 °C–260 °C. At 30 °C, all samples display an incomplete single semicircular arc with large radii, indicating the insulating behavior of ceramics. It is clear that the radii of semicircular arcs decrease continuously with increasing of doping concentration, meaning an enhancement of conductivity with x. Upon increasing the temperature, all samples exhibit the negative temperature coefficient of resistance behavior for which

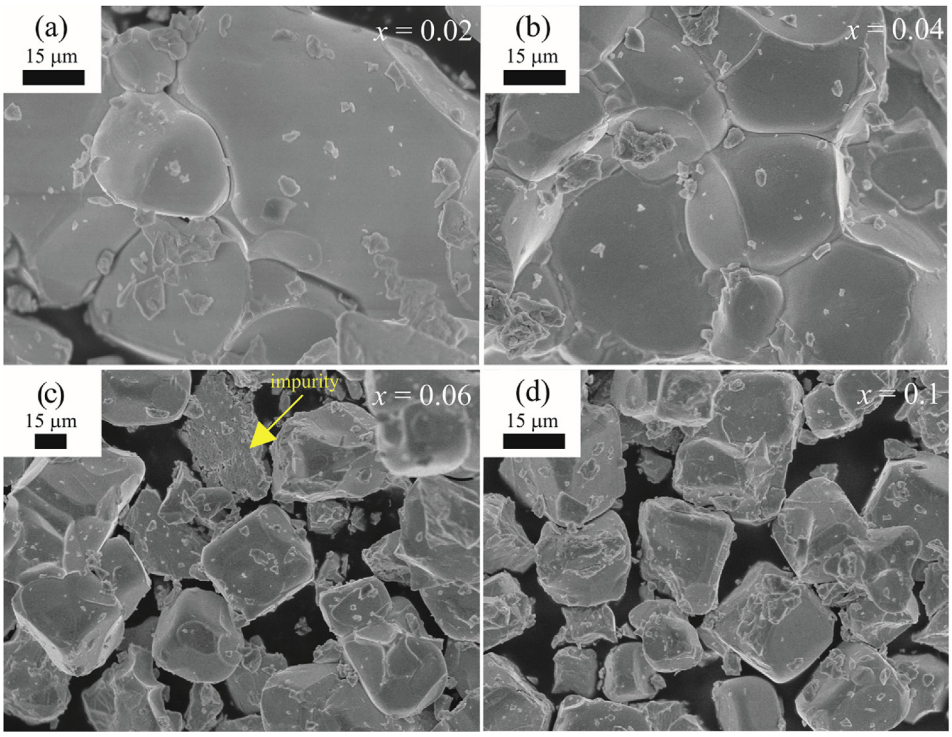

Fig. 6. SEM micrographs of BSFCO samples (a) $x = 0.02$, (b) $x = 0.04$, (c) $x = 0.06$, (d) $x = 0.1$.

the conductivity is found to increase with the increase of temperature. In addition, two semicircular arcs are obviously observed at the temperature above 140 °C, 100 °C, and 50 °C for samples $x = 0.02$ and 0.04, 0.06, and 0.1, respectively. The emergence of the second arc clearly depends on the temperature and frequency. For instance, the second arc starts to appear at 5 kHz and 140 °C or 11 kHz and 180 °C for the sample $x = 0.02$, and 13 kHz and 100 °C or 41 kHz and 180 °C for the sample $x = 0.06$, as clearly denoted in Fig. 7. In general, the high frequency semicircular arc represents the contributions from grains, while the low frequency arc is related to the grain boundary effects. Therefore, it is clear that the resistivity of the BSFCO ceramic samples are involved in hopping electron of the grains at room temperature, and both grain and grain boundary are contributed to the resistivity at high temperatures [46]. Due to a continuous suppression of the high frequency semicircular arc, we suspect that the grain boundary resistance may dominate at higher temperatures, while the grain resistance value reduces to zero. The previous studies on the impedance of BFO-based compounds revealed three distinct relaxation mechanisms. Firstly, a single semicircular arc corresponding to the grain relaxation was observed over the entire temperature and frequency range in the work of Wang et al. [47]. Secondly, the grain and grain boundary relaxations are contributed mainly to the impedance spectra of composites of 0.9BFO-0.1$BaTiO_3$ and 0.73BFO-0.27$PbTiO_3$ [46,48]. Thirdly, grain boundary relaxation was observed at high temperature region, while both the grain and grain boundary contributed to the electrical properties at the lower temperature, even at room temperature [49,50]. In general, the coexistence of the grain and grain boundary relaxations is believed to originate from the oxygen vacancies [46,48–50]. We therefore suggest that a high conductivity of Bi-rich $Bi_{14}CrO_{24}$ impurity phase could be responsible for the impedance spectra of BSFCO compounds. It is worth mentioning that the centers of semicircular arcs are below the Z′-axis indicating the existence of non-Debye type relaxation in BSFCO compounds.

The influence of structural evolution on the magnetic properties of BSFCO compounds are shown in Fig. 8. The hysteresis loops of samples $x = 0.02$–0.08 are clearly shown very narrow loops with finite remanent magnetization (M_r) and coercivity field (H_c), while an improvement of ferromagnetic behavior was observed for $x = 0.1$ with the larger magnetization, M_r, and H_c. The measured M_r and H_c values are respectively about 0.01 emu/g and 0.33 kOe for $x = 0.02$–0.08, and 0.06 emu/g and 1.22 kOe for $x = 0.1$, which are a remarkable higher than that of bulk BFO. The occurrence of the weak ferromagnetism in BSFCO compounds approves the antiferromagnetic ordering of (Sm, Cr) codoped BFO. It is accepted that the enhanced ferromagnetism in doped BFO can be achieved by suppressing (or destroying) the initial partially modulated spin structure, which is respectively correlated with the structural distortion (distorted *R3c* structure) or structural transformation [27–30,34,51–53]. Although the cycloidal spin structure can be unlocked, the net magnetic moments arising from canting of the antiferromagnetic sublattices only gives a weak ferromagnetism. Several research groups have claimed that doping BFO with transition metals can enhance the magnetic properties due to the superexchange interactions between dopant ions or dopant and Fe ions [54,55], especially, the chemical ordering of Fe and Cr in the B-site was theoretically predicted in $BiFe_{0.5}Cr_{0.5}O_3$ [56–58]. However, the hysteresis loops in Fig. 8 obviously shows no evidence of cation ordering, ferrimagnetism, or double-exchange mechanism. We therefore believe that the structural evolution plays an important role in the change of magnetic properties of BSFCO compounds. Our comments are in good agreement with the previous reports [25,30]. Thus, the variation tendency of the magnetization in Fig. 8 is now understood in terms of the phase coexistence of the spiral G-type antiferromagnetic and collinear G-type antiferromagnetic orderings [59]. In samples $x = 0.02$–0.08, the collinear antiferromagnetic of the $PbZrO_3$-type structure is a minority phase as compared to the cycloidal spin structure of the *R3c* phase, as seen in Table 1. Hence, the hysteresis loops observed

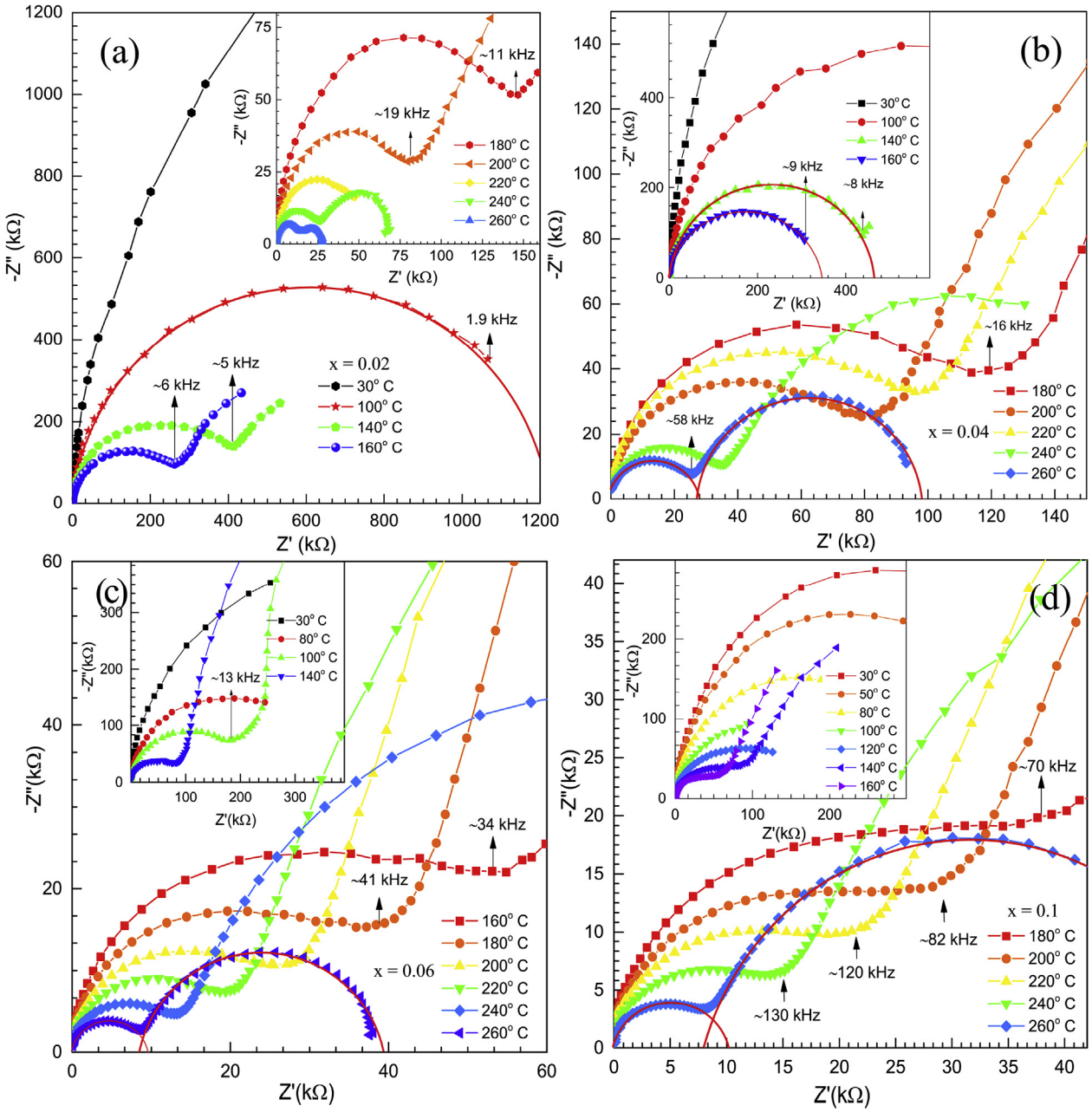

Fig. 7. Cole-Cole (Nyquist) plot of impedance of BSFCO samples with (a) $x = 0.02$, (b) $x = 0.04$, (c) $x = 0.06$, (d) $x = 0.1$.

in these samples are mainly contributed from the intrinsic magnetic behavior of the *R3c* phase. The enhancement of magnetization observed in sample $x = 0.1$ is due to an increase in $PbZrO_3$-type/*R3c* phase ratio in a whole mass. Interestingly, the substitution of Cr for Fe does not suppress the cycloidal spin structure in the *R3c* symmetry as evident from the hysteresis loops of samples $x = 0.02–0.08$. According to the Raman scattering spectra studies, the decrease of tilt angle takes effect on the weakening of Dzyaloshinskii–Moriya interactions, and thus Cr doping on the Fe-site cannot reveal the weak ferromagnetism in the *R3c* phase. A similar manner was previously observed in BFO doping with Mn [28]. The role of Cr^{3+} ions in the Fe^{3+} magnetic sublattices is not clear, but it may extend the modulation period as observed with Sm [60] and Mn [61]. Further investigations are required in order to understand the influence of Cr^{3+} on the cycloidal spin structure.

4. Conclusions

In summary, we reported on the structural, vibrational, electrical and magnetic properties of $Bi_{0.9}Sm_{0.1}Fe_{1-x}Cr_xO_3$ ($0.02 \leq x \leq 0.1$) ceramics. Analysis of the crystal structure reveals the polymorphs of the *R3c* rhombohedral and $PbZrO_3$-type orthorhombic symmetries, along with $Bi_{14}CrO_{24}$ impurity. The Rietveld refinement using either the *Pbam* or *Pnam* orthorhombic symmetry produced comparable fitting quality that we could not identify as a correct symmetry of the $PbZrO_3$-type orthorhombic structure through Rietveld method. The analysis of Raman scattering spectra further confirms the phase coexistence and non-magnetic $Bi_{14}CrO_{24}$ impurity. The Cole-Cole plots show the coexistence of the grain and grain boundary relaxations. The magnetic properties of compounds are mainly related to the intrinsic magnetic behavior

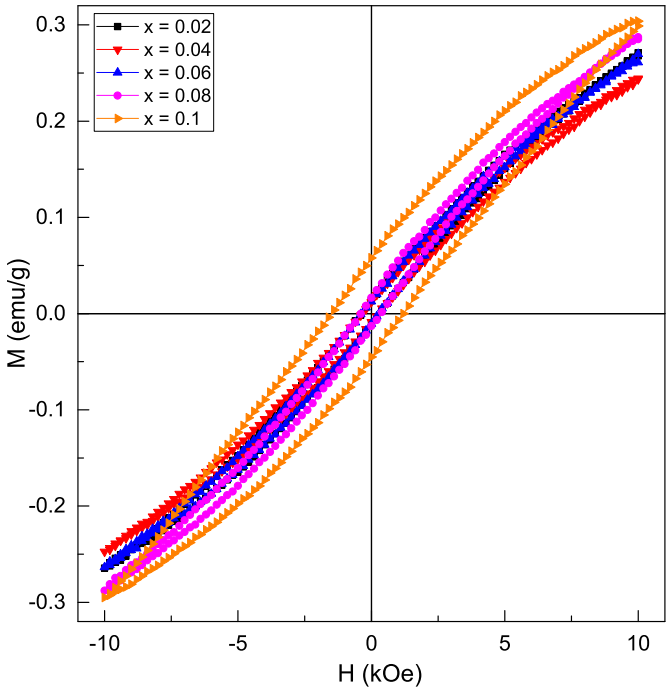

Fig. 8. Hysteresis loops of BSFCO compounds at room temperature.

of the spiral G-type antiferromagnetic (*R3c* phase) and collinear G-type antiferromagnetic orderings ($PbZrO_3$-type structure). The cation ordering, ferrimagnetism, and double-exchange mechanism, on the other hand, did not show any contribution to the magnetic properties of our samples.

Acknowledgements

This research is funded by Vietnam National Foundation for Science and Technology Development (NAFOSTED) under grant number 103.02-2019.22, and funded by the Ministry of Education and Training, Vietnam (B2019-TNA-03.VL).

References

[1] J. Chen, H. Huang, H. Liu, L. Fan, J. Deng, L.-Q. Chen, X. Xing, Y. Ren, Z. Pan, Phys. Rev. Lett. 120 (2018) 55501.
[2] C.J. Cheng, D. Kan, S.H. Lim, W.R. McKenzie, P.R. Munroe, L.G. Salamanca-Riba, R.L. Withers, I. Takeuchi, V. Nagarajan, Phys. Rev. B. 80 (2009) 014109.
[3] P. Liermann, P. Dera, M. Somayazulu, Z. Wu, P. Ganesh, Y. Ren, M. Ahart, R.E. Cohen, H. Mao, R.J. Hemley, Nature 451 (2008) 545.
[4] F. Xue, L.-Q. Chen, D. Song, Q. Zhang, J. Zhu, W. Sun, J.-F. Li, Z. Liao, Phys. Rev. B 95 (2017) 214101.
[5] R. Guo, L.E. Cross, S.-E. Park, B. Noheda, D.E. Cox, G. Shirane, Phys. Rev. Lett. 84 (2000) 5423.
[6] D. Damjanovic, J. Am. Ceram. Soc. 88 (2005) 2663.
[7] D. Damjanovic, Appl. Phys. Lett. 97 (2010) 1.
[8] I.O. Troyanchuk, D.V. Karpinsky, M.V. Bushinsky, V.A. Khomchenko, G.N. Kakazei, J.P. Araujo, M. Tovar, V. Sikolenko, V. Efimov, A.L. Kholkin, Phys. Rev. B 83 (2011) 054109.
[9] D. Kan, L. Pálová, V. Anbusathaiah, C.J. Cheng, S. Fujino, V. Nagarajan, K.M. Rabe, I. Takeuchi, Adv. Funct. Mater. 20 (2010) 1108.
[10] X.X. Shi, X.Q. Liu, X.M. Chen, J. Appl. Phys. 119 (2016) 064104.
[11] H. Liu, J. Chen, L. Fan, Y. Ren, L. Hu, F. Guo, J. Deng, X. Xing, Chem. Mater. 29 (2017) 5767.
[12] T.H. Le, N.V. Hao, N.H. Thoan, N.T.M. Hong, P.V. Hai, N.V. Thang, P.D. Thang, L.V. Nam, P.T. Tho, N.V. Dang, X.C. Nguyen, Ceram. Int. 45 (2019) 18480.
[13] V.A. Khomchenko, J.A. Paixão, V.V. Shvartsman, P. Borisov, W. Kleemann, D.V. Karpinsky, A.L. Kholkin, Scr. Mater. 62 (2010) 238.
[14] P.T. Tho, N.X. Nghia, L.H. Khiem, N.V. Hao, L.T. Ha, V.X. Hoa, C.T.A. Xuan, B.W. Lee, N.V. Dang, Ceram. Int. 45 (2019) 3223.
[15] P.T. Tho, E.M. Clements, D.H. Kim, N. Tran, M.S. Osofsky, M.H. Phan, T.L. Phan, B.W. Lee, J. Alloy. Comp. 741 (2018) 59.
[16] P.T. Tho, D.H. Kim, T.L. Phan, N.V. Dang, B.W. Lee, J. Magn. Magn. Mater. 462 (2018) 172.
[17] I.O. Troyanchuk, D.V. Karpinsky, M.V. Bushinsky, O.S. Mantytskaya, N.V. Tereshko, V.N. Shut, J. Am. Ceram. Soc. 94 (2011) 4502.
[18] A. Siddaramanna, V. Kothai, C. Srivastava, R. Ranjan, J. Phys. D Appl. Phys. 47 (2014) 045004.
[19] V. Kothai, R. Prasath Babu, R. Ranjan, J. Appl. Phys. 114 (2013) 114102.
[20] S.R. Das, R.N.P. Choudhary, P. Bhattacharya, R.S. Katiyar, P. Dutta, A. Manivannan, M.S. Seehra, J. Appl. Phys. 101 (2007) 034104.
[21] M.A. Basith, A. Billah, M.A. Jalil, N. Yesmin, M.A. Sakib, E.K. Ashik, S.M.E. Hoque Yousuf, S.S. Chowdhury, M.S. Hossain, S.H. Firoz, B. Ahmmad, J. Alloy. Comp. 694 (2017) 792.
[22] P.T. Tho, N.V. Dang, N.X. Nghia, L.H. Khiem, C.T.A. Xuan, H.S. Kim, B.W. Lee, J. Phys. Chem. Solids 121 (2018) 157.
[23] J. Walker, P. Bryant, V. Kurusingal, C. Sorrell, D. Kuscer, G. Drazic, A. Bencan, V. Nagarajan, T. Rojac, Acta Mater. 83 (2015) 149.
[24] C.J. Cheng, A.Y. Borisevich, D. Kan, I. Takeuchi, V. Nagarajan, Chem. Mater. 22 (2010) 2588.
[25] X.X. Shi, X.Q. Liu, X.M. Chen, Adv. Funct. Mater. 27 (2017) 1604037.
[26] D.V. Karpinsky, I.O. Troyanchuk, A.V. Trukhanov, M. Willinger, V.A. Khomchenko, A.L. Kholkin, V. Sikolenko, T. Maniecki, W. Maniukiewicz, S.V. Dubkov, M.V. Silibin, Mater. Res. Bull. 112 (2019) 420.
[27] E. Gil-González, A. Perejón, P.E. Sánchez-Jiménez, M.A. Hayward, J.M. Criado, M.J. Sayagués, L.A. Pérez-Maqueda, J. Alloy. Comp. 711 (2017) 541.
[28] V.A. Khomchenko, I.O. Troyanchuk, M.I. Kovetskaya, J.A. Paixão, J. Appl. Phys. 111 (2012).
[29] X. Lu, M. Zeng, L. Yang, X. Gao, K.H. Lam, J. Gao, C. Wang, A. Zhang, M. Qin, Z. Li, Ceram. Int. 43 (2017) 12764.
[30] M. Kubota, K. Oka, H. Yabuta, K. Miura, M. Azuma, Inorg. Chem. 52 (2013) 10698.
[31] D. Errandonea, D. Santamaria-Perez, S.N. Achary, A.K. Tyagi, Solid State Commun. 182 (2014) 50.
[32] B. Guo, H. Deng, X. Zhai, W. Zhou, X. Meng, G. Weng, S. Chen, P. Yang, J. Chu, Mater. Lett. 186 (2017) 198.
[33] F. Lin, Q. Yu, L. Deng, Z. Zhang, X. He, A. Liu, W. Shi, J. Mater. Sci. 52 (2017) 7118.
[34] Y.U. Idzerda, W.S. Chang, C.W. Yu, J.-M. Lee, P.-Y. Chen, C.-S. Chen, C.-S. Tu, Y. Ting, J. Am. Ceram. Soc. 101 (2017) 883.
[35] D.A. Rusakov, A.M. Abakumov, K. Yamaura, A.A. Belik, G. Van Tendeloo, E. Takayama-Muromachi, Chem. Mater. 23 (2011) 285.
[36] H. Yan, R.M. Wilson, K. Zhou, C. Yu, V. Koval, D. Zhang, G. Viola, I. Abrahams, A. Mahajan, N.V. Tarakina, J. Eur. Ceram. Soc. 38 (2017) 1374.
[37] J. Hlinka, J. Pokorny, S. Karimi, I.M. Reaney, Phys. Rev. B 83 (2011) 020101.
[38] J. Bielecki, P. Svedlindh, D.T. Tibebu, S. Cai, S.-G. Eriksson, L. Börjesson, C.S. Knee, Phys. Rev. B. 86 (2012) 184422.
[39] V. Koval, I. Skorvanek, J. Durisin, G. Viola, A. Kovalcikova, P. Svec, K. Saksl, H. Yan, J. Mater. Chem. C 5 (2017) 2669.
[40] J. Zhang, Y.J. Wu, X.J. Chen, J. Magn. Magn. Mater. 382 (2015) 1.
[41] J. Zhang, Y.J. Wu, X.K. Chen, X.J. Chen, J. Phys. Chem. Solids 74 (2013) 849.
[42] P. Sharma, S. Satapathy, D. Varshney, P.K. Gupta, Mater. Chem. Phys. 162 (2015) 469.
[43] Y.B. Yao, W.C. Liu, C.L. Mak, J. Alloy. Comp. 527 (2012) 157.
[44] A. Singh, A. Senyshyn, H. Fuess, S.J. Kennedy, D. Pandey, Phys. Rev. B 89 (2014) 024108.
[45] C. Ederer, N.A. Spaldin, Phys. Rev. B 71 (2005) 060401(R).
[46] A. Singh, V. Pandey, R.K. Kotnala, D. Pandey, Phys. Rev. Lett. 101 (2008) 247602.
[47] P. Wang, Y. Pu, Ceram. Int. 43 (2017) S115.
[48] S. Bhattacharjee, V. Pandey, R.K. Kotnala, D. Pandey, Appl. Phys. Lett. 94 (2009) 012906.
[49] H.M. Usama, A. Akter, M.A. Zubair, J. Appl. Phys. 122 (2017) 244102.
[50] A. Srivastava, A. Garg, F.D. Morrison, J. Appl. Phys. 105 (2009) 054103.
[51] X.S. Gao, C.A. Wang, X.B. Lu, M. Zeng, M.H. Qin, H.Z. Pang, J.-M. Liu, A.H. Zhang, J. Phys. D Appl. Phys. 48 (2015) 395302.
[52] P. Kumar, N. Shankhwar, A. Srinivasan, M. Kar, J. Appl. Phys. 117 (2015) 194103.
[53] P. Kumar, M. Kar, J. Alloy. Comp. 584 (2014) 566.
[54] G. Arya, J. Yogiraj, N.S. Negi, J. Shah, R.K. Kotnala, J. Alloy. Comp. 723 (2017) 983.
[55] Y.-S. Chiang, C.-S. Tu, P.-Y. Chen, C.-S. Chen, J. Anthoniappen, Y. Ting, T.-S. Chan, V.H. Schmidt, Ceram. Int. 42 (2016) 13104.
[56] B.R. McBride, J. Lieschke, A. Berlie, D.L. Cortie, H.Y. Playford, T. Lu, N. Narayanan, R.L. Withers, D. Yu, Y. Liu, J. Appl. Phys. 123 (2018) 154104.
[57] D. Ménard, L.-P. Carignan, C. Harnagea, T. Veres, R. Nechache, F. Normandin, A. Pignolet, Appl. Phys. Lett. 89 (2006) 102902.
[58] P. Baettig, N.A. Spaldin, Appl. Phys. Lett. 86 (2005) 012505.
[59] I. Levin, S. Karimi, V. Provenzano, C.L. Dennis, H. Wu, T.P. Comyn, T.J. Stevenson, R.I. Smith, I.M. Reaney, Phys. Rev. B. 81 (2010) 020103(R).
[60] R.D. Johnson, P.A. McClarty, D.D. Khalyavin, P. Manuel, P. Svedlindh, C.S. Knee, Phys. Rev. B. 95 (2017) 054420.
[61] I.O.T.I. Sosnowska, W. Schäfer, W. Kockelmann, K.H. Andersen, Appl. Phys. Mater. Sci. Process 74 (2002) S1040.